Chapter 13
Photometric Stereopsis for 3D Reconstruction of Space Objects

Xue Iuan Wong, Manoranjan Majji, and Puneet Singla

Abstract The use of photometric stereopsis approaches to estimate the geometry of a resident space object (RSO) from image data is detailed. The set of algorithms and methods for shape estimation form an integral element of a Dynamic Data Driven Application System (DDDAS) for enhancing space situational awareness, where, sensor tasking and scheduling operations are carried out based upon the RSO orbital and geometric attributes, as estimated from terrestrial and space-based sensor systems. Techniques for estimating the relative motion between successive frames using image features are used for data alignment before surface normal estimation. Mathematical models of photometry and imaging physics are exploited to infer the surface normals from images of the target object under varied illumination conditions. Synthetic images generated from physics based ray-tracing engine are used to demonstrate the utility of the proposed algorithms.The proposed framework results in a estimates of the surface shape of the target object, which can subsequently used in forward models for prediction, data assimilation and subsequent sensor tasking operations. Sensitivity analysis is used to quantify the uncertainty of reconstructed surface.

13.1 Introduction

Space situation awareness (SSA), including space surveillance and characterization of all space objects and environments, is critical for national and economic security. SSA is the ability to detect, track and characterize passive and active space objects. In light of the large number of resident space objects, (RSOs, > 20,000) and the

---

X. I. Wong (✉) · P. Singla
Department of Mechanical and Aerospace Engineering, University at Buffalo, Buffalo, NY, USA
e-mail: xuewong@buffalo.edu; psingla@buffalo.edu

M. Majji
Aerospace Engineering, Director, Land, Air and Space Robotics Laboratory, Texas A&M University, College Station, TX, USA
e-mail: mmajji@tamu.edu

E. Blasch et al. (eds.), *Handbook of Dynamic Data Driven Applications Systems*,
https://doi.org/10.1007/978-3-319-95504-9_13

generally accepted notion that our knowledge about the number and nature of most of the objects is severely limited to none, an unmet and urgent need exists for accurate tracking and characterization of RSOs. In addition to orbit parameters, RSO shape and size attributes are necessary to characterize long term evolution of the orbital states, especially for objects in the low and mid Earth orbital regimes. Dynamic Data Driven Application Systems (DDDAS) provide an important avenue to monitor resident space objects, by enabling mechanisms to infer their shape, state and number, and simultaneously providing a data driven feedback loop about which future measurements are to be made to maintain the RSO uncertainties in the catalog below acceptable threshold values. Such a framework comprises of an interplay between various algorithms and methods, catering to different SSA products. Figure 13.1 provides a notional overview of such a system called *INFOrmation and Resource Management (INFORM)* conceived by the authors for SSA applications.

An important aspect of space exploration and situational awareness involves the characterization of surface geometry of space objects. Surface geometry estimates are then utilized by the forward models for uncertainty propagation and subsequent resource allocation operations for catalogue maintenance, conjunction assessment and other SSA product generation. While astronomers are more interested in measuring the geometry of natural space objects such as asteroid and planetoids, the measurement of man-made objects such as spacecraft enable better characterization of resident space objects of interest in space situational awareness applications.

Common methods applied in space object's surface measurement are based on stereo vision [22], laser scanning [6], and photoclinometry [26]. Traditional methods of binocular stereopsis [11, 32] estimate the 3D shape of an object by triangulating image feature correspondences from two or more images obtained from viewpoints. Determination of pixel correspondences across multiple images

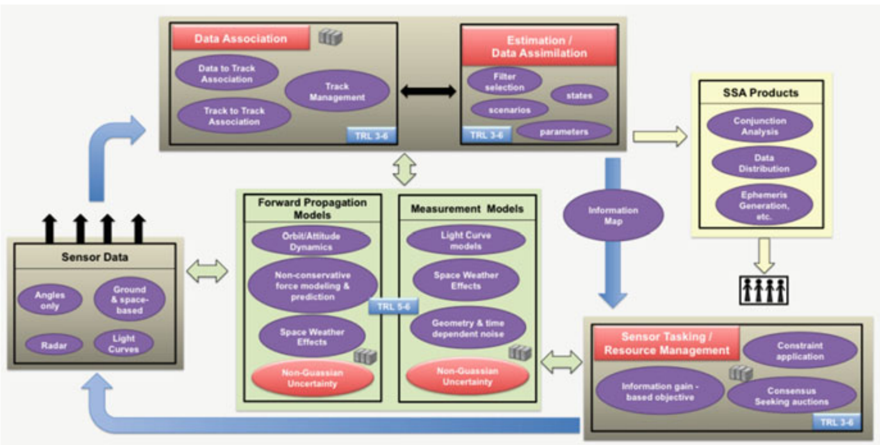

Fig. 13.1 INFORM framework: A DDDAS for SSA applications

is accomplished by extracting feature points in images and matching with the aid of descriptors. Binocular stereopsis or its multiview counterparts cannot provide a dense surface reconstruction of bland, textureless surfaces. An example for application of stereopsis in surface measurement is the Chinese Chang-E II lunar probe mission [22]. A series of images taken during the lunar probe landing process are used to recover 3D map of the landing zone. In this process, the measurements at different position but roughly along the same direction are used in conjunction with an adaptive Markov field algorithm [29] to recover pixel correspondences for dense surface reconstruction. In addition to being computationally expensive, multiview stereo techniques require high resolution imagery to establish feature correspondences. In RSO images with ground or space based telescopes, it is difficult to acquire images at high resolution with a finite depth of field. Light Detection and Ranging (LIDAR) is a time of flight measurement system that scans a collimated LASER to obtain range measurements. Ḃeing a reliable approach for surface scanning, LIDARs are widely used in space missions. For example, the measurement of Mercury's terrain in MESSENGER mission were obtained through LIDAR [6]. The need for specialized instrumentation obviates the use of LIDARs for shape estimation of RSOs.

Photoclinometry, also known as "shape from shading" is an approach for estimating surface shape of space objects. Unlike the other methods discussed previously, shape from shading does not directly measure surface geometry but estimates surface slope. The central idea behind photoclinometry is to infer shape by exploiting the dependence of surface slope on the intensity gradient of the surface in an image. Light reflection on a surface is governed by the reflectance model, or photometric function, which is a function of the geometry, surface material properties, and illumination (light polarity, wave length, incidence angle, etc.). Surface geometry given by the gradient may be parameterized in terms of the azimuth and polar angles with respect to a body fixed coordinate system. Since photoclinometry has an intensity measurement for each surface point, the estimates of surface slope from single image is an underdetermined problem. In order to solve surface gradient from the given information, photoclinometry defines additional constraints such as brightness and smoothness to provide regularity for the estimation problem. Given the illumination condition and an image that captures the reflected light of a surface, photoclinometry estimates surface gradients based on a reflectance model. Surface gradients are then integrated to estimate local surface geometry. The advantage of photoclinometry is the capability of reconstructing a high resolution surface with a finite set of images of comparable resolution. However, due to the requirement of constraint equations, photoclinometry can only estimate local geometry of a smooth surface up to certain accuracy. Practical applications utilize it as a source of auxiliary information for data assimilation with other measurements of surface geometry.

Photometric stereo [15] uses image observations of an object from various illumination conditions to deduce the shape and reflectance characteristics of the object. Similar to shape from shading, photometric stereo infers surface gradients from reflectance model and light measurements. In comparison to photoclinometry, photometric stereo does not require the definition of extra constraint equations to make this inference. Additional image requirements made with the same relative pose under variant illumination conditions are used in lieu of the photoclinometry constraints. Photometric stereo provides better accuracy in estimating surface gradients. In SSA applications, where the telescope observations of a target are available, it becomes the method of choice for shape estimation and forms the basis for shape estimation in the INFORM DDDAS framework. Photometric stereo has the same disadvantage as photoclinometry in terms of the fact that only surface gradients are estimated. Surface shape has to be estimated through spatial integration, which suffers from quality degradation when surface discontinuities exist. Thus for mapping applications, photometric stereo technique is less practical as compared to traditional texture based stereo technique. Image observations of an object also carry relative pose information. Structure from motion algorithms provides the basis for deriving relative pose estimates from image features. To this end, we ask the following question: *given a sequence of images of a space object, how do we utilize photometric stereo to provide high resolution surface reconstructions along with camera relative pose estimates?*

Application of photometric stereo has been confined to controlled laboratory environment, owing to various limitations. First, photometric stereo requires a controlled illumination environment. In various outdoor environments, lighting is usually uncontrollable [1, 40]. In the space environment however, the Sun is the predominant light source, with known reference location.

A key challenge associated with photometric stereo is related to establishing pixel correspondences. Within the controlled environment where there is no relative motion between camera and object, pixel correspondences can be directly established by comparing pixel entries uniformly across different frames. In case of uncontrollable environment, when the object is allowed to move relative to the camera, this assumption is violated and one cannot assign contiguous pixel patches to belong to the same parts of the object across different frames. To solve this problem, multi-view photometric stereo [13] introduces the concepts from the multi-view stereo [34] to first estimate a rough surface and then iteratively optimize a cost function based upon the error between the estimate surface normal and depth gradient. Method proposed by Higo [14] attempts to solve for both object shape and normal vector simultaneously by posing an optimization problem that estimates a best fitting surface to attain to photometric consistency. Another multi-view stereo method developed by Zhou [41] focuses on materials with isotropic reflection (identical diffuse constant). A set of iso-depth contours [2] are first estimated from images and the 3D position of a sparse set of surface points are determined through the application of structure from motion methods. A complete surface reconstruction is then accomplished by propagating depth from determined surface points along the iso-depth contour. Passive photometric stereo [21] also makes use of structure from motion methods to first determine set of sparse surface points. Instead of propagating depth from surface points, they estimate a piecewise planar surface and then iteratively corrects this surface until it converges.

The INFORM based DDDAS approach for shape estimation is similar to Zhou's method [41] and passive photometric stereo [21]. It utilizes structure from motion methods to estimate a sparse set of surface points. Estimation of an iso-contour line is not necessary in our formulation. Further, the assumption of isotropic surface is also relaxed. We also obviate the necessity to construct a piecewise linear surfaces for iterative corrections. The INFORM based DDDAS method to estimate RSO surface geometry starts by applying *structure from motion* methods to detect a set of surface points in object space. This accomplishes sparse 3D reconstruction of these surface points. Each of these surface points are projected back into images to recover their reflected intensity along different illumination directions. Photometric stereo is then applied to estimate their surface normals. By assuming distance between two adjacent pixels is small, we then utilize the surface normal estimates to broadcast depth value among the adjacent pixels with finite difference approach. The process of propagating surface point and estimating the local normal vector is repeated until all pixels with valid measurements are traversed. To this end, the algorithm consists of three main steps. (1) Estimating the initial surface point with structure from motion and feature correspondences, (2) Estimating surface normal of aligned pixel patches using photometric stereo, and (3) Estimating dense surface using the depth propagation algorithm. Note that the proposed method does not solve large scale optimization problem iteratively. The surface propagation process being a local function is amenable to parallelization. Therefore, the proposed algorithm is more computationally efficient when compared to most of the multi-view photometric stereo algorithms including passive photometric stereo. The proposed algorithm also does not assume isotropic surface. Therefore, it is more general when compared to Zhou's method [41].

The rest of this chapter is organized as follows. Section 13.2 provides the problem statement. Introduction to photometric stereo is given in Sect. 13.3 and a brief summary of structure from motion method is provided in Sect. 13.4. Section 13.5 develops an algorithm to implement the photometric stereo to estimate 3D surface of RSOs. Section 13.6 details the experiment results. Section 13.7 draws the conclusions on the DDDAS approach.

13.2 Problem Statement and Background

Technical details of the problem statement involving photometric stereopsis are discussed in this section. Assume that sun is the only light source and that the reflected light from planets are neglected. Reflected light from the natural or man-made space object is captured by the imaging system. The sensor system includes a digital imager with appropriate optical elements for imaging process. A similar sensor system for SSA applications is considered by Jia et al. [18]. It is of interest to obtain a 3D reconstruction of the RSO surface from a set of images obtained under different illumination conditions.

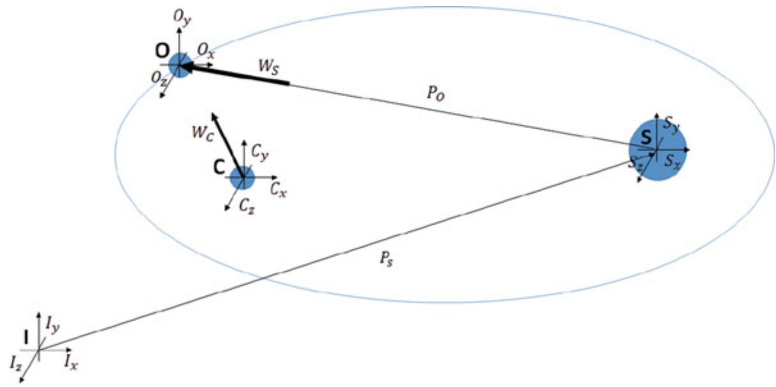

Fig. 13.2 Coordinate systems and geometry of the problem

Photometric stereopsis process mainly comprises of three major components, namely the light source, the object, and the observer. To develop mathematical model associated with imaging process, an inertial frame denoted by I is defined as shown in Fig. 13.2. It is assumed that a point light source with known position with respect to inertia frame is used as the source for the imaging process. Assume that distance between light source and object is large when compared to the size of object, such that object's surface is illuminated by a source at infinity along the vector $\mathbf{w}_s$. The reflected light ray then arrives at object's surface and is assumed to have identical illumination direction over the entire workspace.

Due to the relative motion, object experiences translation and rotation relative to the light source and the observer. Therefore, the light incidence direction with respect to object's surface varies from frame to frame. Assume the object is rotating about its own center of gravity with a rotational velocity of $\omega_{\mathbf{o}}$. The relative orientation R_{OS} is then computed by integrating the following equation with initial attitude, $R_{OS}(t_0)$:

$$\dot{R}_{OS}(t) = -[\omega_o \times] R_{OS}(t) \tag{13.1}$$

$[\omega_o \times]$ is the cross product matrix [33]. The light incidence direction, $\mathbf{w}_s$, on the object's surface is given in the **O** frame by the equation:

$$\mathbf{w}_s(t) = R_{OS}^T(t) \frac{\mathbf{p}_O}{|\mathbf{p}_O|} \tag{13.2}$$

where $\mathbf{p}_O$ is position of the object **O** with respect to the source **S** expressed in the object coordinate system.

Consider an observer **C**, orbiting the object O be described by the vector $\mathbf{p}_c$, the vector $\mathbf{w}_c$ represents the line of sight from the observer to the object. Observation of the object is projected on a 3D image frame that is aligned with the coordinate system that is affixed **C**. We assume that the sensor is located at the observer, with its axes aligned with the coordinates of the observer.

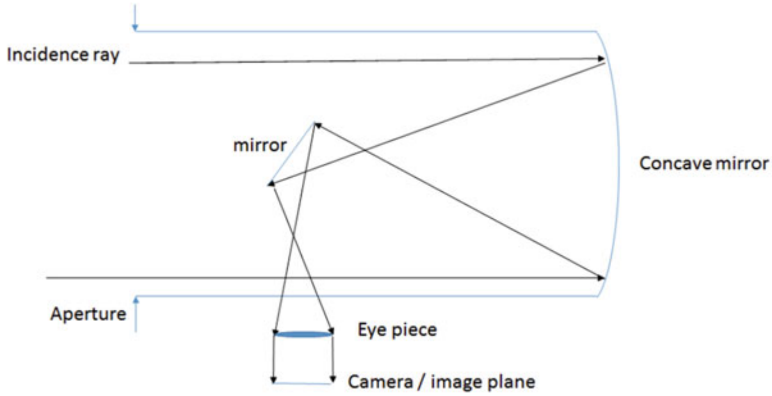

Fig. 13.3 Simplified model of telescopic lens system

Assume that there is a telescopic lens attached to the camera, or a camera with a small field of view. In such optical systems such as telephoto lens, the rays of reflected light from the object to the image are parallel to each other. The light transport physics in the telephoto optics is markedly different from traditional camera systems, where a pin-hole projection model is found to be more appropriate [11]. Telephoto optics are more aptly modeled by utilizing an orthographic projection model.

The telescopic lens model in Fig. 13.3 shows that an orthographic projection simplifies the process of image formation as a close approximation to telescopic lens system. To this end, we assume an orthographic projection model is suitable for SSA applications of interest in this Chapter.

13.3 Photometric Stereo

13.3.1 Formulation

Based on the geometry of the image formation process, we now provide a brief introduction to photometric stereopsis. Assuming a Lambertian reflectance model for the surface [30], the relationship between incidence light direction, $\mathbf{w}_s$ and reflected radiance, l_r is given as:

$$l_r = k_d l_s \mathbf{n}_x \cdot \mathbf{w}_s \tag{13.3}$$

where $\mathbf{n}_x = [n_x, n_y, n_z]$ represents the surface normal vector, k_d is the Lambertian reflectance coefficient, and l_s represents the incidence light radiance. Using the Lambertian reflection model, the magnitude of reflected radiance, l_r, is written as:

$$l_r = k_d l_s (n_x w_{s,x} + n_z w_{s,y} + n_z w_{s,z}), \quad \mathbf{w}_s = [w_{s,x}, w_{s,y}, w_{s,z}] \tag{13.4}$$

Dividing l_r with l_s we define the normalized radiance, $|l|$ (or the gain of the reflection process) as:

$$|l| = \frac{l_r}{l_s} = k_d(n_x w_{s,x} + n_z w_{s,y} + n_z w_{s,z}) \tag{13.5}$$

This can be written as:

$$|l| = k_d[w_{s,x}, w_{s,y}, w_{s,z}][n_x, n_y, n_z]^T \tag{13.6}$$

Given at least three measurements of l_r at different incidence illumination directions, one can solve for components of $k_d\mathbf{n}$ in Eq. 13.6 using a system of linear equations. Assuming we have k number of measurements; the linear system of equations is given as:

$$\begin{bmatrix} |l|_1 \\ |l|_2 \\ \cdot \\ \cdot \\ \cdot \\ |l|_k \end{bmatrix} = \begin{bmatrix} w_{s,x,1} & w_{s,y,1} & w_{s,z,1} \\ w_{s,x,2} & w_{s,y,2} & w_{s,z,2} \\ & \cdot & \\ & \cdot & \\ & \cdot & \\ w_{s,x,k} & w_{s,y,k} & w_{s,z,k} \end{bmatrix} \begin{bmatrix} k_d n_x \\ k_d n_y \\ k_d n_z \end{bmatrix} \tag{13.7}$$

Equation 13.7 can be written in the matrix form as:

$$\mathbf{l} = W_s[k_d\mathbf{n}_x] \tag{13.8}$$

where $\mathbf{l} \in \mathbb{R}^{k\times 1}$, $W_s \in \mathbb{R}^{k\times 3}$. The vector $[k_d\mathbf{n}_x]$ is given by the following least squares solution:

$$[k_d\mathbf{n}_x] = (W_s^T M W_s)^{-1} W_s^T M\mathbf{l} \tag{13.9}$$

where M is a weight matrix. Note that the Lambertian model follows a cosine distribution when incidence angle is less than $\pi/2$ rad. It will truncated at zero for any incidence angle larger than $\pi/2$ rad. However, 0 intensity does not necessarily a product of incidence angle larger or equal to $\pi/2$. It could be a result of shadowing or masking. Therefore, we exclude measurements of zero intensity from applying to photometric stereo.

Knowing that the normal vector is a unit vector, $\mathbf{n}$ is therefore normalized direction vector of $[k_d\mathbf{n}]$, and k_d is its length. The reflectance coefficient k_d can therefore be simultaneously estimated.

$$\mathbf{n} = \frac{[k_d\mathbf{n}]}{|[k_d\mathbf{n}]|} \tag{13.10}$$

$$k_d = |[k_d\mathbf{n}]| \tag{13.11}$$

Photometric stereo estimates the surface normal with the least squares solution. Therefore, more consistent measurements leads to a more accurate solution. However, photometric stereo solution is undefined when the coefficient matrix W_s is of rank less than 3. This frequently implies that all of the $\mathbf{w}_s$ lie on the same plane. When all the measurements are distributed on a plane, we do not have enough information to correctly estimate the normal vector for each surface point. In the present INFORM framework, which is a DDDAS for shape estimation of RSOs, the principal light source is the Sun. Variation of intensity of the reflected light is caused by the relative pose of the RSO with respect to the light source. In the event that the relative pose is invariant through the imaging process, the coefficient matrix ceases loses rank. Photometric stereopsis, therefore relies heavily on the observability of the normal vector for each image pixel.

13.3.2 Modified Photometric Stereo

Solving surface normal with linear least square is a simple and elegant approach. However, the solution of the least squares problem involves the use of redundant parameterization of the normal vector components along with the coupling of the reflectance coefficient. Minimal parameterization of the normal vector in terms of azimuth angle and the polar angle is written in Eq. 13.12 as

$$\mathbf{n_x} = \left[\, sin(\xi)sin(\Omega) \;\; cos(\xi)sin(\Omega) \;\; cos(\Omega) \,\right] \tag{13.12}$$

where ξ is azimuth angle, and Ω is polar angle measured in terms of body frame coordinate. Using the definition of the normal vector of Eq. 13.12 and substituting it into the Lambertian model, we get:

$$|l| = k_d \left(w_{s,x} sin(\xi)sin(\Omega) + w_{s,y} cos(\xi)sin(\Omega) + w_{s,z} cos(\Omega) \right) \tag{13.13}$$

We use the Gaussian Least Square differential Correction (GLSDC) algorithm [7] as the non-linear least square solver in this problem to solve for the unknown diffusivity constant, polar angle and azimuth angle. The state vector containing these three unknown is defined as follows:

$$\mathbf{x} = \left[\, k_d \;\; \Omega \;\; \xi \,\right]$$

An interation process for estimating the elements of the state vector $\mathbf{x}$ in the GLSDC is setup to minimize the error functional

$$\Delta y_k = \mathbf{l} - \hat{\mathbf{l}}(\hat{\mathbf{x}}_k) \tag{13.14}$$

where vector $\mathbf{l}$ is intensity measurement, and $\hat{\mathbf{l}}(\hat{\mathbf{x}})$ is predicted intensity vector solved with estimated parameter vector $\hat{\mathbf{x}}$. If the error vector is larger then a given threshold, a differential correction to estimate parameters is applied as:

$$\hat{\mathbf{x}}_{k+1} = \hat{\mathbf{x}}_k + \Delta \mathbf{x}_k \tag{13.15}$$

$$\Delta \mathbf{x}_k = (H_k^T H_k)^{-1} H_k^T \Delta y \tag{13.16}$$

The Jacobian matrix of the Lambertian model with respect to each unknown term is solved about the previous estimated state $\hat{\mathbf{x}}_k$ as:

$$H_k = \left[\frac{\partial |l|}{\partial k_d} \; \frac{\partial |l|}{\partial \Omega} \; \frac{\partial |l|}{\partial \xi} \right]_{\hat{\mathbf{x}}_k} \tag{13.17}$$

$$\frac{\partial |l|}{\partial k_d} = w_{s,x} sin(\xi) sin(\Omega) + w_{s,y} cos(\xi) sin(\Omega) + w_{s,z} cos(\Omega)$$

$$\frac{\partial |l|}{\partial \Omega} = k_d (w_{s,x} sin(\xi) cos(\Omega) + w_{s,y} cos(\xi) cos(\Omega) - w_{s,z} sin(\Omega))$$

$$\frac{\partial |l|}{\partial \xi} = k_d (w_{s,x} cos(\xi) sin(\Omega) - w_{s,y} sin(\xi) sin(\Omega))$$

Differential corrections of Eq. 13.15 are applied until the norm of the error vector Δy_k of Eq. 13.14 drops below a pre-defined threshold value or the error change between two successive iterations gets small. Do note that when the polar angle is equal to zero, term $\frac{\partial |l|}{\partial \xi}$ is equal to zero as well. This indicates that we lose observability on the azimuth angle when polar angle is equal to zero. Losing observability in azimuth angle does not affect the final solution, but causes singularity when solving correction term with Eq. 13.16. A simple solution to avoid such a problem is to drop the terms related to azimuth angle when polar angle equals zero:

$$H = \begin{cases} \left[\frac{\partial |l|}{\partial k_d} \; \frac{\partial |l|}{\partial \Omega} \; \frac{\partial |l|}{\partial \xi} \right] & \Omega \neq 0 \\ \left[\frac{\partial |l|}{\partial k_d} \; \frac{\partial |l|}{\partial \Omega} \right] & \Omega = 0 \end{cases} \tag{13.18}$$

An appropriate choice for the measurement sensitivity matrix can be when the estimated value is sufficiently small, near convergence. Modified photometric stereo is different from original photometric stereo in terms of usage of the non-linear model and the parametrization of normal vector. Given identical measurement sets and using the Lambertian surface assumption, both algorithms yield the same result. Therefore, if computing predicted uncertainty is not required, it is unnecessary to replace original photometric stereo with modified photometric stereo. The point of using modified photometric stereo is to remedy the fact that normal vector directly estimated from original photometric stereo is subject to unit vector constraint, which makes the uncertainty calculations more complex as compared to the two angle parametrization.

Without explicitly relying on the surface normal's unit vector constraint as in traditional photometric stereo, modified photometric stereo is also compatible with more complex photometric function such as the Lunar-Lambert model traditionally applied in photoclinometric methods. In this Chapter, we focuses on developing a framework that has the flexibility in choice of the photometric function, and therefore will restrict our discussions to Lambertian model. However, we note that proposed algorithm is also compatible with other photometric functions, and it is expected to yield better estimation results when applying better choice of photometric functions for various surfaces.

13.3.3 Surface Reconstruction and Depth Estimation

After solving for the normal vector for each pixel on an image, we obtain a normal map that indicates the local normal vector. Rendering of normal map allows to reconstruct appearance of the object at different illumination conditions under fixed view-point direction. For INFORM framework and its utility in the DDDAS for SSA product generation, a 3D surface map is desired. To recover a 3D surface from normal map, a common method is to integrate the surface gradient [9, 20]. Defining two components of the surface gradient as:

$$p = \frac{\partial z}{\partial x}$$

$$q = \frac{\partial z}{\partial y}$$

where p and q indicate surface gradient along x and y direction, respectively. The normal vector is related to surface gradient through:

$$\mathbf{n} = \frac{[p, q, 1]}{\sqrt{p^2 + q^2 + 1}}$$

Therefore, surface gradient may be recovered from the normal vector estimates by making use of the following relationships:

$$p = \frac{n_x}{n_z} \tag{13.19a}$$

$$q = \frac{n_y}{n_z} \tag{13.19b}$$

Assume that position x and y of a surface point are available in the object space. The depth of each surface point is then propagated from adjacent surface point the using finite difference operator given as follows:

$$
\begin{aligned}
z_{u,v} = \tfrac{1}{4}((z_{u+1,v} - \tfrac{(p_{u+1,v}+p_{u,v})\delta x}{2}) \\
+(z_{u-1,v} + \tfrac{(p_{u-1,v}+p_{u,v})\delta x}{2}) \\
+(z_{u,v+1} - \tfrac{(q_{u,v+1}+q_{u,v})\delta y}{2}) \\
+(z_{u,v-1} + \tfrac{(q_{u,v-1}+q_{u,v})\delta y}{2}))
\end{aligned}
\tag{13.20}
$$

where δx and δy are the deflection along x, y directions on the surface.

If the surface is smooth, following the integrability constraint (Eq. 13.21), propagation of depth from each direction should return identical results.

$$
\frac{\partial^2 z}{\partial x \partial y} = \frac{\partial^2 z}{\partial y \partial x} \tag{13.21}
$$

Assumption of integrability will only work on a smooth surface. In most real objects, there are surface discontinuity that leads to violation of this assumption. Propagating the depth value across discontinuous sections leads to erroneous surface reconstruction. Therefore, it is essential to identify surface discontinuities before proceeding to the integration.

Wang [38] proposes to detect discontinuities using three subsequent operations. First, the angles between a pixel and four of its adjacent pixels are computed to establish a threshold to detect a discontinuity. A non-photorealistic (NPR) camera [31] (a method to re-render an image in a non-photorealistic way but to represent a boundary or occlusion) is then applied to input images for depth edge detection. Finally, feature detection techniques are applied on color coded normal map (Rendering an image by coloring each element in normal vector with RGB color) to detect discontinuity in color gradients. Once the discontinuities are detected, reconstruction process will simply have to avoid them during integration to resolve error caused by discontinuity.

Another solution to this problem is to integrate the normal map by imposing integrability constraints through regularization [16]. A quadratic regularization proposed by Horn [16] is to search for a surface that minimizes the following function:

$$
\epsilon(\hat{z}) = \int\int [\nabla \hat{z}(x, y) - [p, q]]^2 dxdy \tag{13.22}
$$

where $\hat{z}$ is the estimated depth. Equation 13.22 can be approximated by the following discrete form:

$$
\epsilon(\hat{z}) = \sum\sum \left[\frac{z_{u+1,v} - z_{u,v}}{\delta x} - \frac{p_{u+1,v} + p_{u,v}}{2}\right]^2 + \left[\frac{z_{u,v+1} - z_{u,v}}{\delta y} - \frac{q_{u,v+1} + q_{u,v}}{2}\right]^2 \tag{13.23}
$$

Minimizing Eq. 13.23 in Euler form by setting $\nabla\epsilon = 0$ leads to the following expression:

$$z_{u,v} = \frac{z_{u+1,v} + z_{u-1,v} + z_{u,v+1} + z_{u,v-1}}{4} - \frac{p_{u+1,v} + p_{u,v} + q_{u,v+1} + q_{u,v}}{8} \tag{13.24}$$

Since all depth values are unavailable initially, Eq. 13.24 sets initial depth to zero and updates the estimated surface iteratively. An improved scheme of this method to include boundary conditions, and an extension into other regularization method is proposed by Horn [16].

Integrating surface normals to derive a depth estimate is an open research problem in computer graphics. This is because most of the proposed methods can not effectively deal with a surface discontinuity, due to the limited information about an object's surface with observations from a single view-point direction. In this chapter, we propose to reconstruct surface by sequentially solving the photometric stereo and normal vector integration problems. This requires accurate estimates of both normal vector and surface point location to proceed. Our solution to this problem depends on the fact that we have a sparse set of surface points with known positions distributed on the object's surface. Let each of these surface points serve as reference points and broadcast the depth value toward entire surface. If there is discontinuity detected along path of propagation, we will simply stop going any further and let other broadcast processes estimate the location of surface point from other sides of the discontinuity. This method allow us to bypass some of the discontinuities in the surface. Although there is no guarantee that proposed method uniformly resolves issues associated with surface discontinuities due to the information available, this method allows us to minimize the error in surface reconstruction.

Having introduced photometric stereo for estimation of surface normals from a sequence of images captured under different illumination directions, we have looked at a modified photometric stereo that allows more efficient computation of the sensitivity terms. This forms an integral element of shape estimation methods in INFORM SSA framework. However, until this point, we have assumed that the relative motion between camera and object is stationary. Therefore, there is no problem in establishing pixel correspondences. In realistic situations, relative motion always exists and therefore establishing pixel correspondences can be fairly difficult. In order to solve this problem, we will first introduce structure from motion methods that allow the recovery of relative pose estimates in addition to rough shape. Rough shape estimation process form sparse feature correspondences is known as sparse stereo.

13.4 Photometric Stereo in Motion

To resolve the issue of relative motion between the camera and the object, we now develop a framework that combines structure from motion algorithms with photometric stereo. There are two stages of the photometric stereo in motion

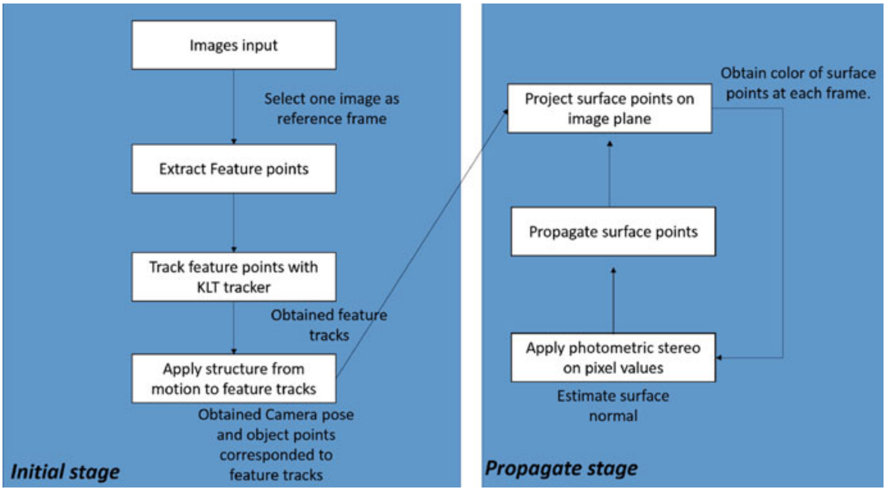

Fig. 13.4 A flow chart for proposed photometric stereo in motion algorithm

algorithm. An initialization stage for estimating the initial condition for the relative pose. This is followed by a propagation stage for estimating the dense 3D surface. During the initialization stage, Scale Invariant Feature Transformation (SIFT) [23] is first applied to detect a set of feature points in the reference image. Each of this feature is then tracked over subsequent sequence with the KanadeLucasTomasi (KLT) tracker [24] to form set of feature tracks. Object space coordinates and the orientation of each image frame with respect to reference image frame are estimated by the application of structure from motion methods on corresponding feature tracks. During our study, a factorization method [36] is being applied as the structure from motion method that provide relative pose and sparse structure estimation. Normal vector of each surface points is then estimated with photometric stereo by using intensity of feature track as input. Set of estimated surface points with the normal vector now defines the initial conditions for the propagation stage.

The propagation stage defines pixels with known object space coordinates and associated normal vector as base pixels, and defines their adjacent pixels that are without either position or normal vector as forward pixels. During propagation, each surface point are propagated spatially to these forward pixels from the base pixel with finite difference method that will be introduced in subsequent discussion. Projecting propagated surface points onto each image with the orthographic model recovers their measured reflected intensity in the image frame. Knowing the pixel value of the projected surface point, photometric stereo is then applied to estimate normal vector from all forward pixels. With both normal vector and location in object space determined, a forward pixel is now updated to be a base pixel. The propagation process is repeated until there are no valid pixels (pixel value > 0) in the image. A flow chart summarizing this algorithm is given in Fig. 13.4.

Note that for each frame in the image sequence, the proposed algorithm does not require any iteration process at the pixel level or surface level. We also do not require expensive pre-computations, therefore we conclude our proposed algorithm yields better computational efficiency in comparison to other algorithms. Since photometric stereo is solved explicitly at each pixel location, there no necessity to assume an isotropic surface.

Propagation of the surface points for orthographic projected image assuming unit distance between surface points corresponding to two adjacent pixels, required us to assume that surface slope remain constant in between two adjacent surface points:

$$z_{u+1,v} = z_{u,v} + \frac{\partial z_{u,v}}{\partial u} du \tag{13.25}$$

Surface slope is recovered using sparse Eq. 13.19. During its application, the term n_z in normal vector can be close to zero and may lead to errors in computing the correct surface slope. When this condition occurs, the propagation process is stopped.

We assume unit distance between pixels, therefore $du = dv = 1$. Since this number does not indicate real displacement between surface points, the reconstructed surface has scale ambiguity. Proposed method can sequentially update surface point location and surface point normal vector at each pixels from any pixel that has valid surface point and normal vector information. Note that this process is highly parallelizable and depth corresponding to various pixel patches may be inferred simulataneously.

13.5 Covariance Analysis

To predict the precision of reconstruction, a commonly used technique is to evaluate the uncertainty of estimated result by considering error and noise introduced from different sources. The method for computing error covariance in this research is based on sensitivity analysis of each participated algorithm.

Figure 13.5 is a roadmap for uncertainty propagation of proposed algorithms, that form a key element of the DDDAS. It illustrates propagation of uncertainty from one module to another. Since outputs of one algorithm form inputs to other algorithms, the uncertainty analysis can be inferred as the sensitivity of the algorithm's output with respect to input uncertainty. The remainder of this section derives the sensitivity analysis of each component, starting from raw sensor noise and ultimately compute the error covariance of reconstructed surface. Note that the error covariance of feature track, and Factorization's shape and motion matrix are derived in a parallel paper by the authors [39].

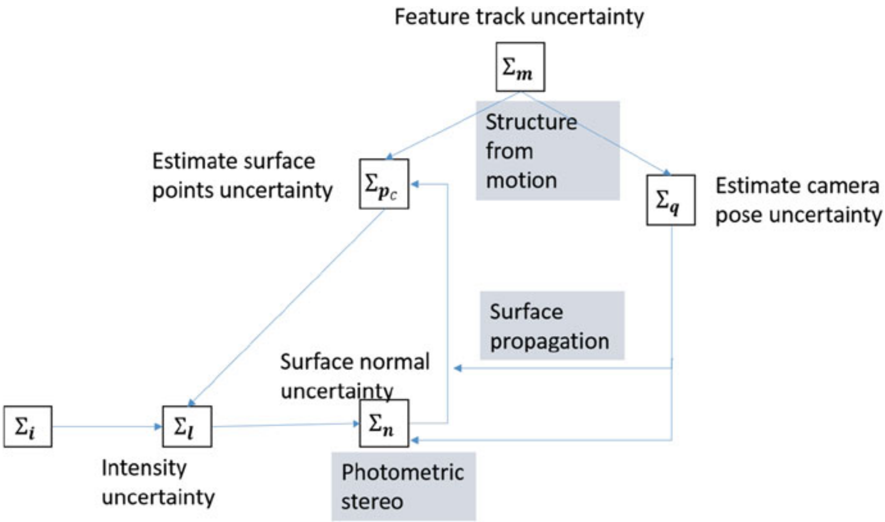

Fig. 13.5 Covariance analysis flowchart. Starting form the error covariance of feature track($\Sigma_{\mathbf{m}}$), it is propagated to the covariance of camera pose ($\Sigma_{\mathbf{q}}$) and the covariance of initial surface point ($\Sigma_{\mathbf{p}_c}$) through structure from motion method. Error covariance of the normal vector($\Sigma_{\mathbf{n}}$) is a function of the covariance of the measurement intensity($\Sigma_{\mathbf{l}}$), and covariance of the camera pose. Uncertainty of measured intensity is related to the image noise covariance($\Sigma_{\mathbf{i}}$), and error caused by projection of surface points on image plane. Uncertainty of surface points and normal vector is propagated toward other surface points through surface propagation process

13.5.1 Raw Sensor Noise and the Intensity Uncertainty

Raw sensor noise includes image noise and the uncertainty associated with the uncertainty of the camera's intrinsic parameters. The orthgraphic projection model has image noise alone. The perspective projection model has uncertainties associated with both image and camera intrinsic parameters. Intrinsic parameter uncertainty may be obtained from the camera calibration process [4].

Image noise is measured with Immerkaer's method [17], which estimates the image noise variance by taking the difference of two Laplacian of the images. It can be shown that the estimation of noise using this method involves a convolution operation with the following kernel:

$$C = \begin{bmatrix} 1 & -2 & 1 \\ -2 & 4 & -2 \\ 1 & -2 & 1 \end{bmatrix} \tag{13.26}$$

A global image noise standard deviation is then computed by:

$$\sigma_i = \sqrt{\frac{\pi}{2}} \frac{1}{6(w-2)(h-2)} \sum |l(x, y) * C| \tag{13.27}$$

where w and h are the width and height of the image. To obtain local intensity variance, w and h with size of a local window are used. These calculations initialize the covariance analysis of subsequent image operations.

13.5.2 Covariance of the Normal Vector Estimates

Using our definition of modified photometric stereo, uncertainties of the estimated polar angle and azimuth angle are first computed. Covariance of the normal vector is then solved using these parameters. Equation 13.16 therefore directly serves as the sensitivity of estimated parameters, with respect to the variation of intensity.

Other than intensity, estimation of the normal vector and diffuse constant k_d also depend on light source direction. Light source direction corresponding to each frame is estimated from image frame orientation with respect to the reference frame. Since the light source depends on estimated value carrying uncertainty, it is also a random variable. It is necessary to compute the sensitivity of the estimated parameter with respect to the light source direction. Using Eq. 13.16 that solves for the sensitivity of the parameter with respect to the intensity variation, sensitivity with respect to the light source direction is calculated using following expressions:

$$\frac{\partial \mathbf{x}}{\partial \mathbf{w}_i} = \frac{\partial \mathbf{x}}{\partial |l|} \frac{\partial |l|}{\partial \mathbf{w}_i} \tag{13.28}$$

$$\frac{\partial |l|}{\partial \mathbf{w}_i} = k_d \mathbf{n} \tag{13.29}$$

$$\frac{\partial \mathbf{x}}{\partial |l|} = (H^T H)^{-1} H^T \tag{13.30}$$

where matrix H is the Jacobian matrix obtained using Eq. 13.18. Error covariance of the estimated surface's azimuth angle and polar angle, along with diffuse constant are then approximated using the following expression:

$$\Sigma_{\mathbf{x}} = \begin{bmatrix} H & \frac{\partial \mathbf{x}}{\partial \mathbf{w}_i} \end{bmatrix} \begin{bmatrix} \Sigma_{\mathbf{I}} & 0 \\ 0 & \Sigma_{\mathbf{w}_i} \end{bmatrix} \begin{bmatrix} H^T & \frac{\partial \mathbf{x}}{\partial \mathbf{w}_i}^T \end{bmatrix}^T \tag{13.31}$$

where $\Sigma_{\mathbf{w}_i}$ is uncertainty covariance of light source direction and $\Sigma_{\mathbf{I}}$ is uncertainty covariance of measurement intensity. During the propagation phase, $\Sigma_{\mathbf{I}}$ will has to consider uncertainty caused by error in estimated camera frame orientation and error in the propagated surface depth. This is because we use this information to acquire the intensity by the back projection technique. Sensitivity of the intensity with respect to camera frame orientation and surface depth can be modeled by using local intensity gradient. However, since there is no guarantee that the projection error is small enough for approximating the local sensitivity information, we use an unscented transform [19] to approximate the intensity measurement uncertainty.

We assume that there is an error in estimating the camera pose and the surface point location. It result in an error in the projection coordinates on the image plane and then causes subsequent error in intensity measurements. Since there is an intensity measurement corresponding to each image plane coordinate, the variance of measurement intensity can be measured as the intensity variation within a region bounded by an area specified by projected image plane location error. The projected image plane location error is estimated by first selecting a set of sigma points, and solving for their projected coordinates on the image. Bounding areas are computed as a rectangle with length equal to maximum distance between projected sigma points.

Light source direction is transformed by utilizing the rotational matrix $R^{(i)}$ at ith frame. Since orientation of the camera is estimated through factorization, results from out recent research provide the corresponding estimation error covariance $\Sigma_{\mathbf{q}}$. Where, orientation of the camera at each frame is parametrized using the Classical Rodrigoues Parameters (CRP),$\boldsymbol{q} = [q_1, q_2, q_3]^T$ [33]. The rotation matrix in terms of CRP is written as:

$$R = \frac{1}{\sqrt{1+\boldsymbol{q}^T\boldsymbol{q}}}\begin{bmatrix} 1+q_1^2-q_2^2-q_3^2 & 2(q_1q_2+q_3) & 2(q_1q_3-q_2) \\ 2(q_1q_2-q_3) & 1-q_1^2+q_2^2-q_3^2 & 2(q_2q_3+q_1) \\ 2(q_1q_3+q_2) & 2(q_2q_3-q_1) & 1-q_1^2-q_2^2+q_3^2 \end{bmatrix} \tag{13.32}$$

Each image frame is a measurement of object at different orientation. Collecting all n measurement frames into a vector $\mathbf{q}$:

$$\mathbf{q} = [\boldsymbol{q}^{(1)}, \boldsymbol{q}^{(2)}, \ldots, \boldsymbol{q}^{(n)}] \tag{13.33}$$

where $\boldsymbol{q}^{(j)}$ indicates the CRP of the jth frame. The light source direction $\mathbf{w}_i^{(n)}$ at each frame expressed in terms of the image space coordinate using the rotational matrix $R^{(n)}$ and light source direction expressed in the reference frame $w_i^{(0)}$ is written as:

$$\mathbf{w}_i^{(n)} = R^{(n)}\mathbf{w}_i^{(0)}$$

Substituting into Eq. 13.32 and taking partial derivatives leads to:

$$\frac{\partial w_{i,x}}{\partial \boldsymbol{q}} = \frac{\partial}{\partial \boldsymbol{q}}R_{11}(\boldsymbol{q})w_{i,x}^0 + \frac{\partial}{\partial \boldsymbol{q}}R_{12}(\boldsymbol{q})w_{i,y}^0 + \frac{\partial}{\partial \boldsymbol{q}}R_{13}(\boldsymbol{q})w_{i,z}^0 \tag{13.34}$$

$$\frac{\partial w_{i,y}}{\partial \boldsymbol{q}} = \frac{\partial}{\partial \boldsymbol{q}}R_{21}(\boldsymbol{q})w_{i,x}^0 + \frac{\partial}{\partial \boldsymbol{q}}R_{22}(\boldsymbol{q})w_{i,y}^0 + \frac{\partial}{\partial \boldsymbol{q}}R_{23}(\boldsymbol{q})w_{i,z}^0 \tag{13.35}$$

$$\frac{\partial w_{i,z}}{\partial \boldsymbol{q}} = \frac{\partial}{\partial \boldsymbol{q}}R_{31}(\boldsymbol{q})w_{i,x}^0 + \frac{\partial}{\partial \boldsymbol{q}}R_{32}(\boldsymbol{q})w_{i,y}^0 + \frac{\partial}{\partial \boldsymbol{q}}R_{33}(\boldsymbol{q})w_{i,z}^0 \tag{13.36}$$

The partial derivative of each rotation matrix elements with respect to CRPs are computed from Eq. 13.32. Error covariance of the light source direction is then propagated from the uncertainty of estimated camera orientation CRP using:

$$\Sigma_{\mathbf{w}_i} = \frac{\partial \mathbf{w}_i}{\partial \boldsymbol{q}} \Sigma_{\boldsymbol{q}} \frac{\partial \mathbf{w}_i}{\partial \boldsymbol{q}}^T \tag{13.37}$$

where $\frac{\partial \mathbf{w}_i}{\partial \boldsymbol{q}}$ is a matrix with each element computed from Eqs. 13.34, 13.35, 13.36, and $\Sigma_{\boldsymbol{q}}$ is computed from the uncertainty analysis of the corresponding camera pose estimation algorithm. Since the camera orientation at different frames may be assumed to be uncorrelated with each other, error covariance is computed independently for each frame.

Given the uncertainty in estimated normal vector's azimuth angle and polar angle, the normal vector uncertainty is computed from the local sensitivity of Eq. 13.12 as:

$$\Sigma_{\mathbf{n}} = \begin{bmatrix} \frac{\partial \mathbf{n}}{\partial \Omega} & \frac{\partial \mathbf{n}}{\partial \xi} \end{bmatrix} \begin{bmatrix} \sigma_\Omega^2 & \sigma_{\Omega,\xi} \\ \sigma_{\Omega,\xi} & \sigma_\xi^2 \end{bmatrix} \begin{bmatrix} \frac{\partial \mathbf{n}}{\partial \Omega} & \frac{\partial \mathbf{n}}{\partial \xi} \end{bmatrix}^T \tag{13.38}$$

$$\frac{\partial \mathbf{n}}{\partial \Omega} = \begin{bmatrix} sin(\xi)cos(\Omega) \; cos(\xi)cos(\Omega) \; sin(\Omega) \end{bmatrix}$$

$$\frac{\partial \mathbf{n}}{\partial \xi} = \begin{bmatrix} cos(\xi)sin(\Omega) \; -sin(\xi)sin(\Omega) \; 0 \end{bmatrix}$$

where σ_Ω and σ_ξ are the standard deviations of the estimated polar angle and azimuth angle. Since the angles are correlated, the correlation term $\sigma_{\Omega,\xi}$ does not equal to zero, these elements are extracted from $\Sigma_{\mathbf{X}}$ computed by Eq. 13.31. Note that when $\Omega = 0$, we do not have an estimate of ξ and therefore we assume normal vector in this case is not a function of ξ, such that term $\frac{\partial \mathbf{n_x}}{\partial \xi}$ is equal to zero.

13.5.3 Error Covariance of the Surface Points

As outlined in the introduction, our reconstruction process uses the estimates of the normal vectors to propagate the surface points in order to estimate a densely reconstructed surface. Surface points propagation of orthographic configuration only solve for depth, while coordinate along x and y direction are deterministic. The propagation of surface depth along the x direction leads to the following equation:

$$z_{u+1,v} = z_{u,v} + \frac{n_x}{n_z}$$

Sensitivity of the propagated depth is solved using:

$$\delta z_{u+1,v} = \left[1 \ \frac{1}{n_z} \ -\frac{n_x}{n_z^2}\right]\left[\delta z_{u,v} \ \delta n_x \ \delta n_z\right]^T \tag{13.39}$$

Error estimate of the depth can thus be computed using the covariance written as:

$$\sigma_{z,u+1,v}^2 = \left[1 \ \frac{1}{n_z} \ -\frac{n_x}{n_z^2}\right]\begin{bmatrix} \sigma_{z,u,v}^2 & 0 & 0 \\ 0 & \sigma_{n,x}^2 & \sigma_{n,xz} \\ 0 & \sigma_{n,xz} & \sigma_{n,z}^2 \end{bmatrix}\begin{bmatrix} 1 \\ \frac{1}{n_z} \\ -\frac{n_x}{n_z^2} \end{bmatrix} \tag{13.40}$$

where the elements $\sigma_{n,x}^2$, $\sigma_{n,xz}$, and $\sigma_{n,z}^2$ of Eq. 13.40 are computed from estimated normal vector error covariance calculations outlined earlier.

Estimation of the error covariance not only serves as a measure of estimation accuracy, but may also be used as criteria for terminating the surface propagation process. Estimated covariance is computed following the surface point location and normal vector carried out for each pixel. Therefore, uncertainty estimates are available during the propagation process. Since surface propagation is a numerical integration process, error from the previous step is accumulated to subsequent steps. In order to avoid propagating error into the future that leads to larger error, the propagation process on a surface points may be terminated when the error covariance exceeds a certain threshold.

13.6 Simulation and Experiment

Experimental measurement data sets to evaluate the proposed algorithms are generated by using a ray tracer based imaging engine called Space Object Light Attribute Rendering (SOLAR) System. This SOLAR system allows us to implement physically plausible reflectance models of object's surface, along with physical optical systems for realistic camera projection and image formation emulations. The SOLAR system is based on an in-house ray tracing engine. Inter-reflection, light refraction, optical elements modeling, etc. are implemented as software blocks in the renderer. Since ray tracer renders a scene by explicitly tracing the path of light incident on each pixel of camera from the scene, it is computationally expensive when compared to commonly used rasterization techniques applied in computer graphics engines such as OpenGL [27] and DirectX [10]. However, ray tracer engine is more suitable for applications, where physically consistent image formation is important over real time rendering. Therefore, we utilize this engine to generate measurement data for demonstration of our algorithms that utilize space information.

Measurement data sets from two object models are synthesized for demonstration purposes. The Itokawa asteroid model [3] is rendered to provide measurements of natural space object with diffuse surface. The Apollo-Soyuz [5] spacecraft model is implemented to provide measurements of a high specular man-made object with surface discontinuity. The Itokawa model has richer surface feature in comparison to the Apollo model. This allows factorization method to has better performance on Itokawa model. In case of the Apollo model, we assume the existence of painted fiducials on the surface, such that it is able to provide some feature points over a large but smooth surface. Each of the object models are rendered under three different conditions to evaluate the performance of the proposed algorithms. First, both objects are rendered with pure Lambertian model and relative motion between camera and object is held stationary. Subsequent emulation scenario renders both Apollo and Itokawa models using pure Lambertian model, while camera-object relative motion is not stationary to evaluate the performance of proposed photometric stereo in motion algorithms. For the third set of experiments, we use the Oren-Nayar model [28] to render the Itokawa model and generate its synthetic measurement. The Apollo model is rendering with Torrance-Sparrow model [37]. Both of these models are considered as physically plausible reflectance model. While the Oren-Nayar model is a diffuse reflection model for rough surfaces, Torrance-Sparrow is a specular reflection model. This experiment is to evaluate the performance of proposed algorithms when using Lambertian model to approximate more complex and realistic light reflection.

A focused Newtonian telescope model without lens aberrations is implemented in the SOLAR system as the optics attached to the camera to validate assumption of orthographic projection.

13.6.1 Stationary Observation of Lambertian Surface

We use the case of no relative motion between the observer and the object to provide a baseline understanding of photometric stereo performance when ideal conditions are satisfied perfectly (i.e., stationary relative pose during measurement, light source direction at each frame is perfectly known and object is isotropic Lambertian surface). It is assumed that the object is located at inertia frame origin, with the camera frame's negative z axis pointing toward the object centroid. It is assumed that the light source is initially oriented along the direction of $\mathbf{w}_{i,0} = [0, 0.707, 0.707]$ and rotated about z axis for 2π rad over 10 frames.

Three out of ten measurements of Apollo model are shown in Fig. 13.6.

Since camera-object relative pose remains constant throughout measurement sequence, we can directly implement photometric stereo to estimate normal vector at each pixel. A collection of normal vectors for each pixel is stored as a normal map. The normal vectors are colored by following the Blue-Green-Red (BGR) color channel scheme for visualization purposes (Fig. 13.7). Values in x direction are plotted as blue, while the values in y and z directions are plotted in green and red, respectively. The intensity of each color is the magnitude of normal vector component. Since colors do not have negative value, we plot a positive normal map

(a) (b) (c)

Fig. 13.6 3 out of 10 measurements of Apollo model, (**a**) $\mathbf{w}_i = [0, 0.707107, 0.707107]$, (**b**) $\mathbf{w}_i = [0.353553, -0.612372, 0.707107]$, (c) $\mathbf{w}_i = [-0.612372, 0.353553, 0.707107]$

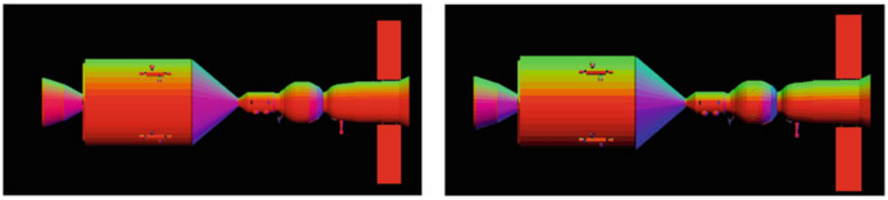

(a) True positive normal Map (b) Estimate positive normal map

Fig. 13.7 A comparison of true positive normal map and photometric stereo estimate positive normal map

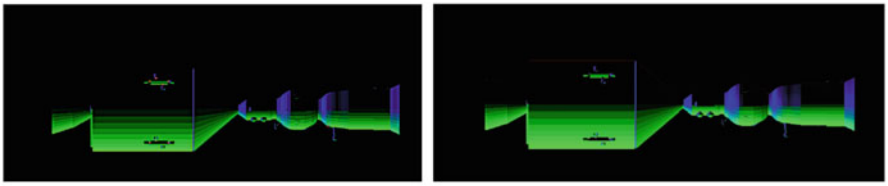

(a) True negative normal Map (b) Estimate negative normal map

Fig. 13.8 A comparison of true negative normal map and photometric stereo estimate negative normal map

that plots only the positive component in a normal vector, and a negative normal map that plots only the negative components of a normal vector (Fig. 13.8).

For better comparison between estimate and true normal map, we define an error function that governs the error between the two normal vector as 1 minus the absolute value of dot product of estimate normal vector, $\mathbf{n}_{est}$ and true normal, $\mathbf{n}_t$:

$$e = 1 - |\mathbf{n}_{est} \cdot \mathbf{n}_t| \tag{13.41}$$

Error of estimated normal vector computed by Eq. 13.41 are visualized as a color map in Fig. 13.9. A visual inspection of the error color map shows that the maximum error is about 0.08 located at regions near the edges of the object. It also shows that

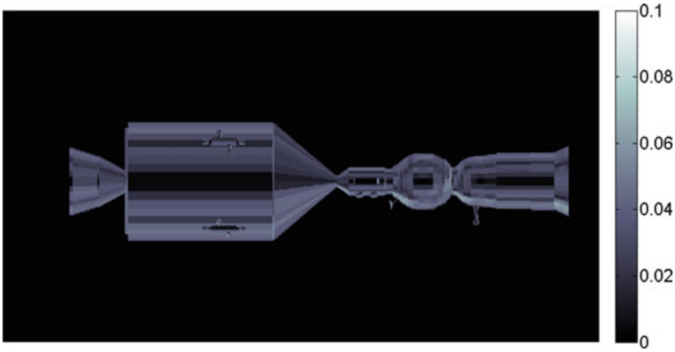

Fig. 13.9 Normal vector estimation error map

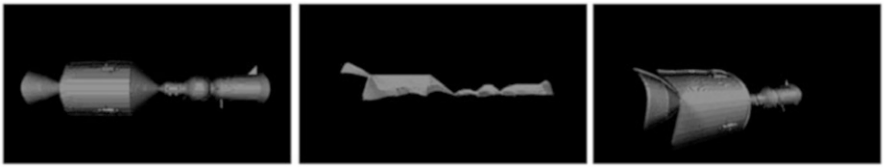

Fig. 13.10 Estimated object surface through normal map integration at different view directions

the surfaces that are oriented along the camera bore-sight have small errors. This experiment result demonstrates that under the ideal conditions, photometric stereo is able to provide good estimates of the surface normal.

Estimation of surface geometry in this experiment is accomplished by integrating surface normal along the surface, starting from an arbitrary initial point with a positive surface depth value.

Figure 13.10 shows estimated surface for the various view of the Apollo model. From these plots, we can infer that the surface estimated from the normal map integration can provide accurate results in areas with smaller surface discontinuities. Automated means of detecting continuous regions in an image remains a research challenge.

Following a similar procedure, we have the estimated normal map for Itokawa model. The normal maps are shown in Figs. 13.11 and 13.12. Normal vector error map is plotted in Fig. 13.13. It is evident that the error levels are equivalent to those of the Apollo model.

Figure 13.14 are snapshots of various views of the estimate surface of Itokawa computed by integrating surface normal map. The estimate surface is poorer than that of the Apollo due to the lack of observability of surface normal at different locations along the edge. On the other hand, the estimated Itokawa surface does not suffer from errors caused by surface discontinuity.

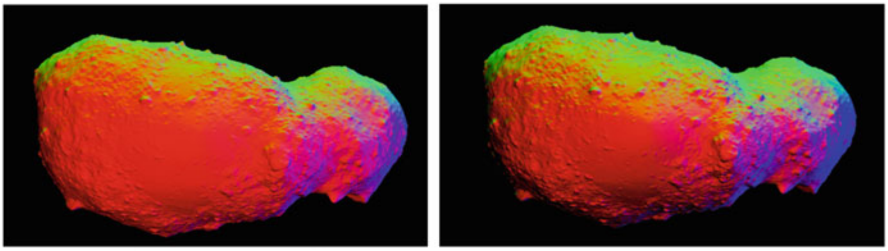

(a) True positive normal Map (b) Estimate positive normal map

Fig. 13.11 A comparison of true positive normal map and photometric stereo estimated positive normal map

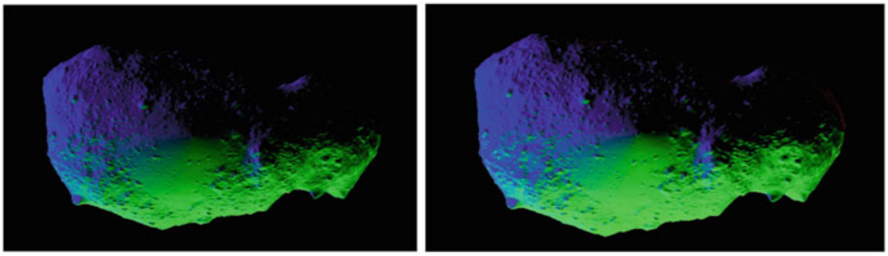

(a) True negative normal Map (b) Estimate negative normal map

Fig. 13.12 A comparison of true negative normal map and photometric stereo estimated negative normal map

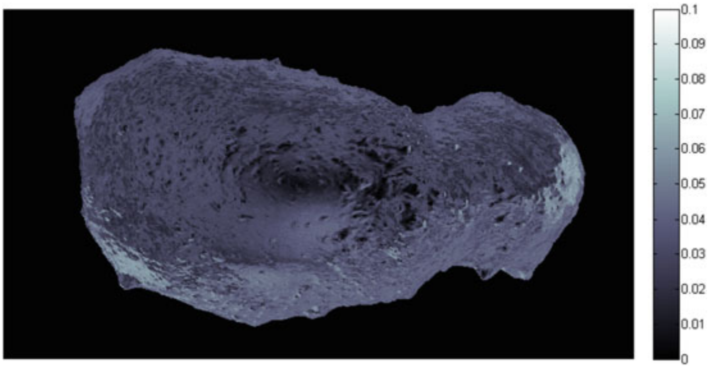

Fig. 13.13 Normal vector estimation error map

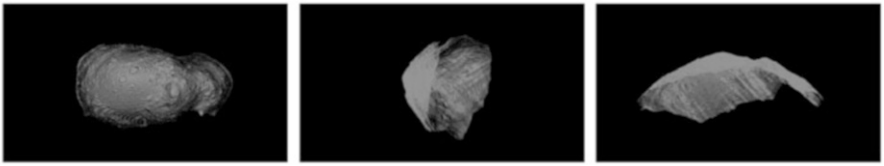

Fig. 13.14 Estimated object surface through normal map integration along different view points

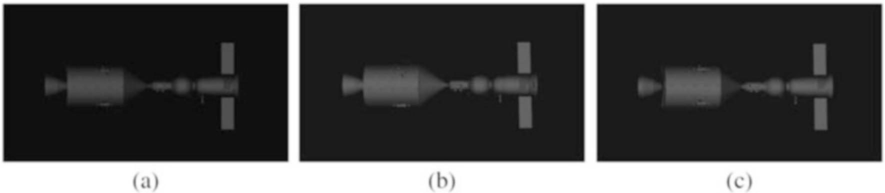

Fig. 13.15 3 out of 50 measurements of Apollo model in motion. (**a**) $\mathbf{w}_c = [0, 0.0, -1]$, (**b**) $\mathbf{w}_c = [-0.1508, -0.1431, -0.9781]$, (**c**) $\mathbf{w}_c = [0.1525, 0.1025, -0.9830]$

Experimental results of this section show that traditional photometric stereo is able to provide good estimates of the surface normal. Surface geometry is then estimated by integrating the estimated surface normal to produce a model for surface geometry.

13.6.2 Observation of Lambertian Surface from Non-stationary View Point

When relative motion between the camera and object is no longer stationary, traditional photometric stereo is not directly applicable. This experiment is to evaluate performance of our photometric stereo in motion approach under assumption that the surface reflectance is Lambertian in nature.

Figure 13.15 show 3 out of 50 measurements of Apollo model. Illumination direction is aligned with view direction in this case because light source is assumed to be affixed in the camera frame. Note that this assumption is not necessary and that the light source direction is free to move around. Set of feature points extracted by SIFT and tracked by KLT tracker in this case are plotted as yellow dots in Fig. 13.16. The red ellipse located at the end of each feature track in Fig. 13.16 are estimated feature track error covariance bound of last feature point in a track. Theses are computed using methods developed by the authors in a related recent research [39].

Feature tracks are supplied to the Factorization algorithm for computing relative pose of each frame. To demonstrate the performance of Factorization, a comparison of estimated orientation with respect to the true camera orientation is shown in Fig. 13.17. Each red and blue dot plotted in Fig. 13.17 indicate the view direction

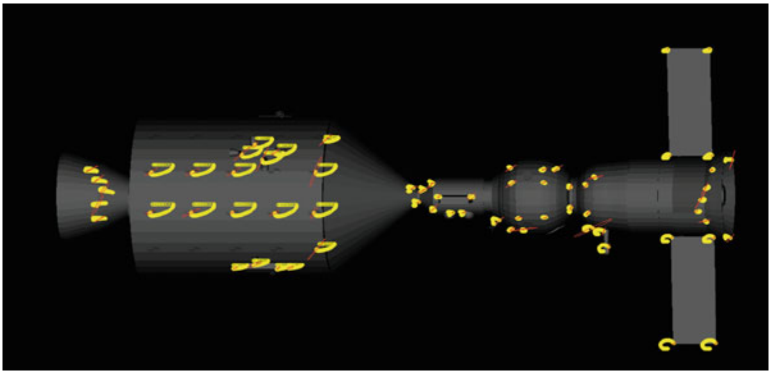

Fig. 13.16 Feature tracks as input to structure from motion method, red ellipse at the end of each track are estiamted uncertainty covariance bound of feature track

Fig. 13.17 A comparison of factorization estimated camera orientation (red dot) and true camera orientation(blue dot) after translated into view direction relative to object

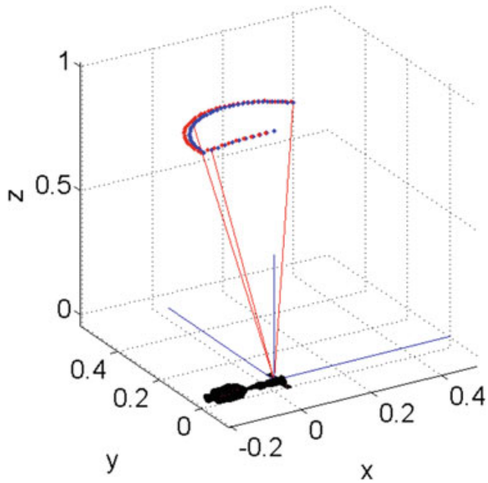

from camera to the object plotted in object fixed frame. This plot shows that factorization method is able to estimate camera orientation with reasonably accuracy.

Using the initial condition provided by the Factorization method, we use the method developed in this work to estimate a surface and normal map for the Apollo model. Estimation results are rendered in Figs. 13.18, 13.19, and 13.20.

The estimated surface in Fig. 13.18 shows that proposed method can provide a reasonable estimate of the surface geometry. Estimation errors incurred in Fig. 13.18 are relatively large when compared to result in Fig. 13.10. This is attributed to the fact that the proposed method works under the non ideal conditions, where the original photometric stereo are not applicable. The reconstructed surface also shows that the proposed method is able to resolve the surface discontinuity issue by making use of additional information from motion alignment of matching pixel patches.

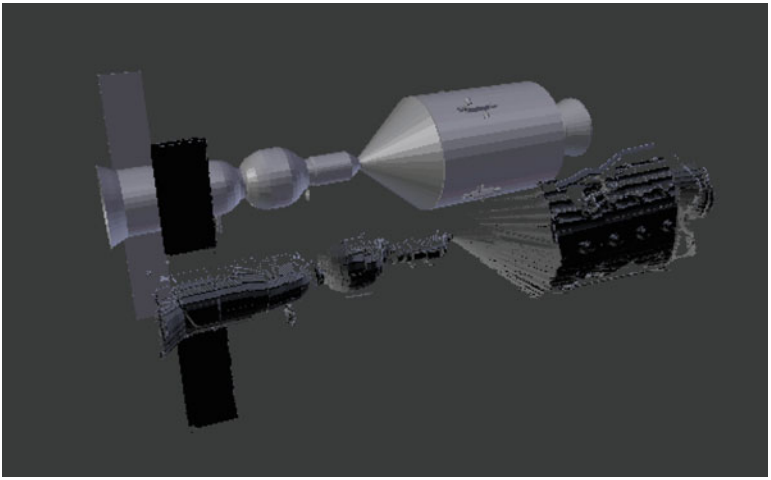

Fig. 13.18 A side to side comparison of estimated space craft surface(front) to true object surface(back). A scaling parameter determined empirically is applied to the estimated surface so that we can compare the estimated surface and true surface in same scale

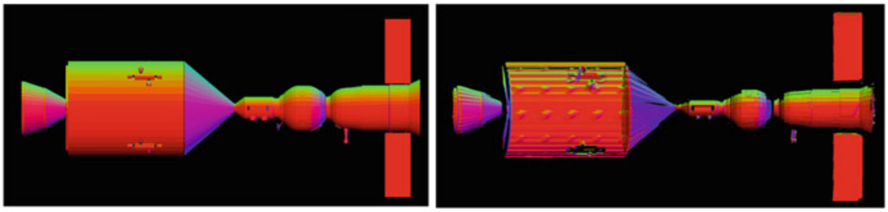

(a) True positive normal Map

(b) Estimate positive normal map

Fig. 13.19 A comparison of true positive normal map and estimated positive normal map of spacecraft model

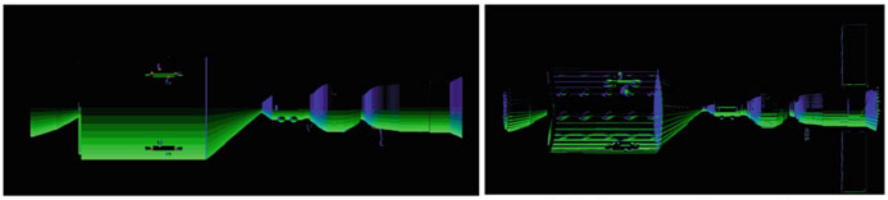

(a) True negative normal Map

(b) Estimate negative normal map

Fig. 13.20 A comparison of true negative normal map and estimated negative normal map of spacecraft model

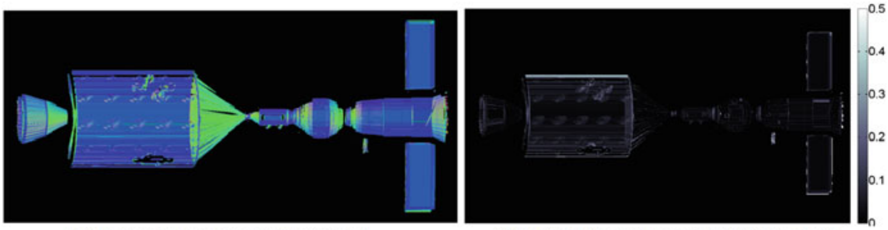

(a) Estimated normal vector uncertainty direction map

(b) Estimated normal vector uncertainty magnitude map

Fig. 13.21 Estimated normal vector uncertainty standard deviation (**a**) direction map (**b**) magnitude map of spacecraft model

A comparison of estimated normal vectors in Figs. 13.19 and 13.20 demonstrates that estimation of surface normal is generally accurate over a large fraction of the surface. Large errors in surface normal estimation occur near the edge of surface segments. This is caused by the error in object points to image projection as the variation of intensity near such region are large, owing to poor observability of depth in orthographic projection.

In addition to the estimation of surface geometry and surface normals, we also derive methods to compute the covariance associated with both the estimates. For visualization purposes, estimation error variance is first translated to standard deviation, and plotted as a color map. In case of the normal vector uncertainty, a direction map and a magnitude map are plotted separately. The direction map indicates the distribution of error in x, y, and z direction within a normal vector. A magnitude map is used to indicate the magnitude of uncertainty of corresponded pixel. Since surface depth is a scalar variable, the surface depth standard deviation map only plots the estimated standard deviation of surface depth value.

Figure 13.21 shows the estimated standard deviation of the estimated normal vector. The direction map indicates that a large fraction of the uncertainty in estimated normal vector is distributed along the direction with minimum magnitude. While the magnitude map indicates large estimation error are concentrated around region closed to the edge. This is equivalent to loss of observability and similar to Fig. 13.22. Figure 13.22 is the estimated standard deviation of the surface depth estimates, patch like distribution of surface depth uncertainty correspond to pixel patches used by the depth estimation algorithm. A poor starting solution depth therefore is propagated to the patch that is computed from that solution.

After examining the performance of the proposed algorithm on a man-made object, we now repeat the experiments on Itokawa asteroid that represents natural space object without surface discontinuity. Three out of a total of 50 input images for Itokawa experiment are shown in Fig. 13.23. Estimated Itokawa surface is shown in Fig. 13.24.

Comparing the estimated surface of Itokawa through proposed method in Fig. 13.24 and from original photometric stereo in Fig. 13.10, we see that estimation

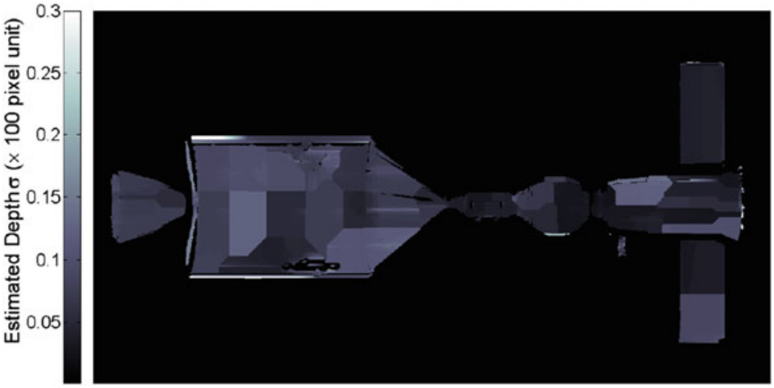

Fig. 13.22 Estimate surface depth standard deviation map of spacecraft model

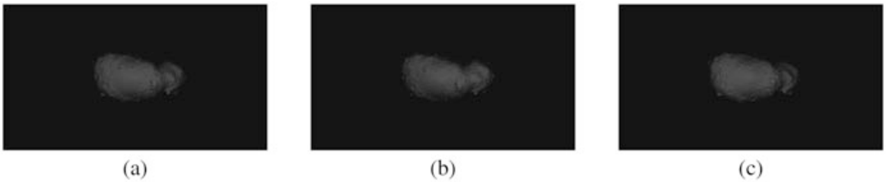

Fig. 13.23 3 out of 50 measurements of Itokawa model in motion. (**a**) $\mathbf{w}_c = [0, 0.0, -1]$, (**b**) $\mathbf{w}_c = [-0.1508, -0.1431, -0.9781]$, (**c**) $\mathbf{w}_c = [0.1525, 0.1025, -0.9830]$

result in case of the motion stereo algorithm is actually better. This can be attributed to the use of large number of observations that yield better observability and improved imaging geometry. This experiment also shows that the concept of using multiple initial surface points estimated from structure from motion method, and then propagated for constructing a dense surface with photometric stereo is indeed feasible.

A comparison of estimation results in Figs. 13.25 and 13.26 shows that the estimation of normal vector with proposed approach fairs better for semi-convex geometries that have contiguous regions. Estimated uncertainties result are graphically rendered in Figs. 13.27 and 13.28.

This set of experiments demonstrate the application of the proposed algorithm in estimating the surface geometry of both man-made and natural objects. Experimental results indicate that performance of proposed approach on a continuous surface is better than performance on a surface with discontinuities. These algorithms demonstrate optimism as elements of the INFORM framework to derive RSO shape estimates as a part of the DDDAS for SSA applications.

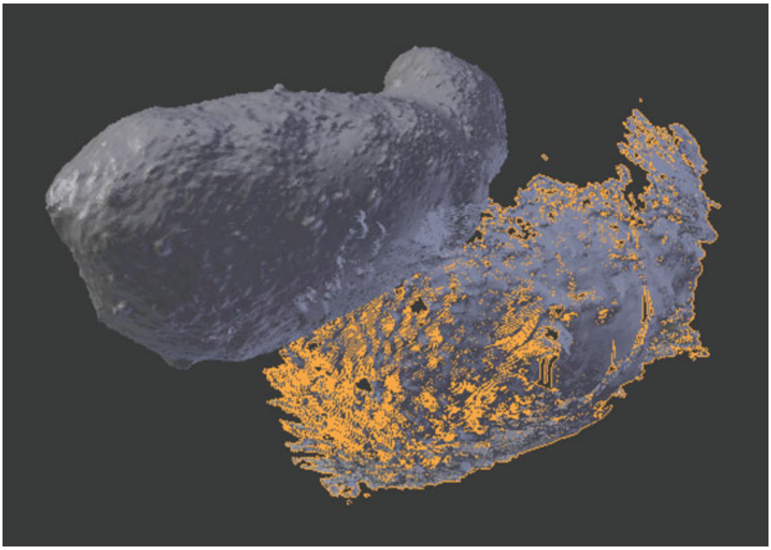

Fig. 13.24 A side to side comparison of empirically scaled Itokawa surface estimates (front) with true object surface (back)

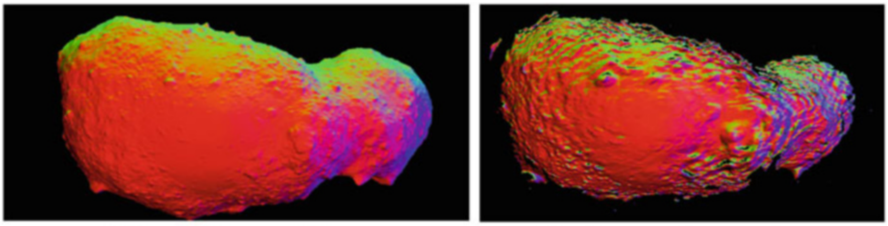

(a) True positive normal Map (b) Estimate positive normal map

Fig. 13.25 A comparison of true positive normal map and estimated positive normal map of an asteroid model

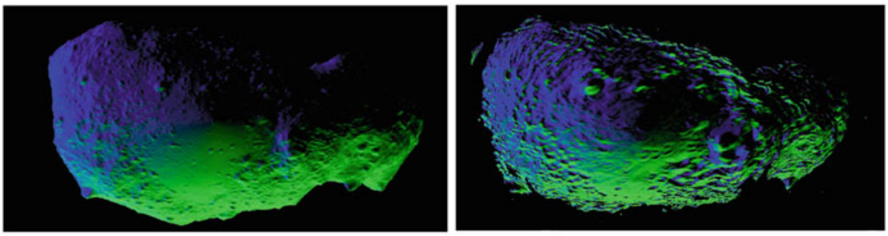

(a) True negative normal Map (b) Estimate negative normal map

Fig. 13.26 A comparison of true negative normal map and estimated negative normal map of an asteroid model

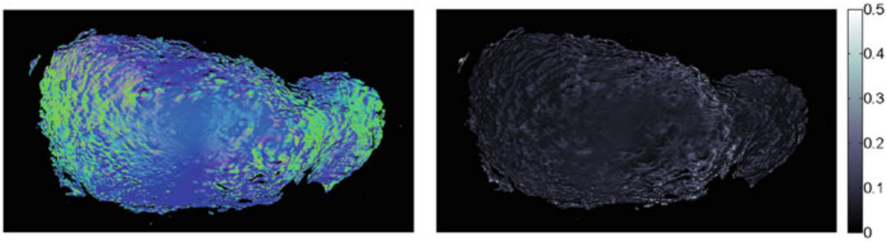

(a) Estimated normal vector uncertainty direction map

(b) Estimated normal vector uncertainty magnitude map

Fig. 13.27 Standard deviation of the estimated normal vector (**a**) direction map (**b**) magnitude map

Fig. 13.28 Estimate surface depth standard deviation map of asteroid model

13.6.3 Observation of Non-Lambertian Surface from Non-stationary View Point

After demonstrating the utility of the proposed algorithms in reconstructing the Lambert surface, we now move on to evaluate the performance of proposed algorithm in reconstruction of non-Lambertian surface.

Man-made space objects are usually coated with materials that have high reflectance in order to reflect heat from radiation. Based on this fact, it is natural to assume that most of the man-made space objects have high specular reflection. Therefore, their reflectance should be modeled with specular reflection models. The Torrance-Sparrow model is considered a physics based specular reflectance model, although it is not as comprehensive as other methods such as HTSG model [12].

Given a set of measurements of Apollo model rendered by Torrance Sparrow model in Fig. 13.29, it is desired to estimate the shape of the object of interest. Direct application of the photometric stereo on measurements with specular component

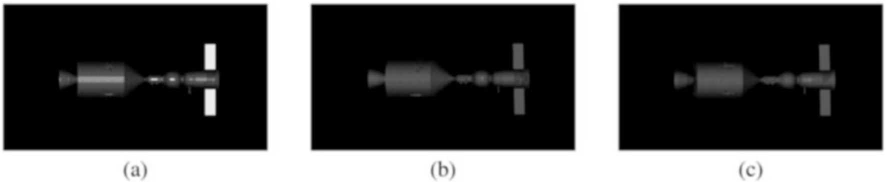

Fig. 13.29 3 out of 100 measurements of Apollo model in motion, (**a**) specular component is clearly brighter than diffuse component. (**b–c**) specular component is not captured because camera direction is off from specular peak direction

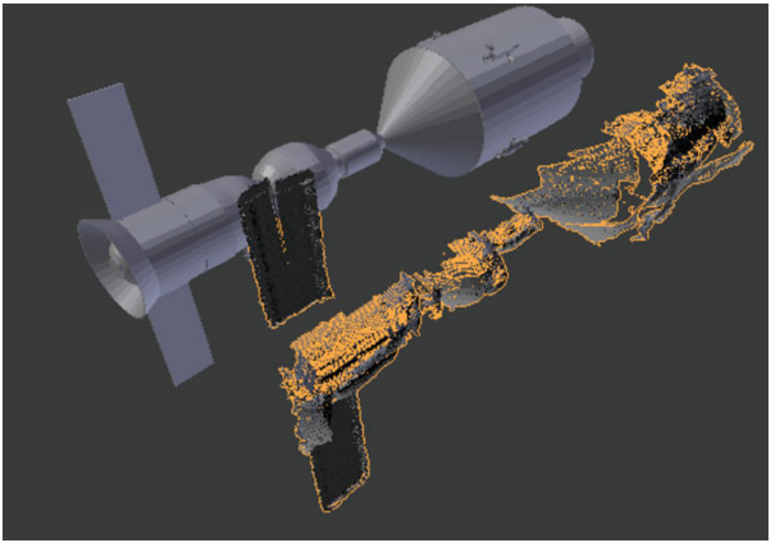

Fig. 13.30 A side to side comparison of empirically scaled estimate Apollo surface (front) to true object surface (back) with measurement rendered with Torrance Sparrow model

will result large error in the estimated normal vector. Therefore, measurements with specular components will need to be removed before the estimation of the normal vector. Since the specular reflection is concentrated around specular peak direction, when there are sufficient number of measurements, the specular component can be removed as outliers. In this experiment, we use RANdom SAmple Consensus (RANSAC) algorithm [8] to search for outlier measurements with specular component and reject them. A downside of using RANSAC is that large amount of measurements are required in order to detect specular reflection. Therefore, we increase the number of image measurements to 100 frames in this experiment. Once the measurements with specular reflections are removed, remaining images are assumed to be purely diffuse and photometric stereo in motion algorithm is applied to estimate the surface geometry.

Figures 13.30, 13.31, 13.32, 13.33, and 13.34 are the depth estimation results of the Apollo model from measurements with specular reflection. Reconstruction

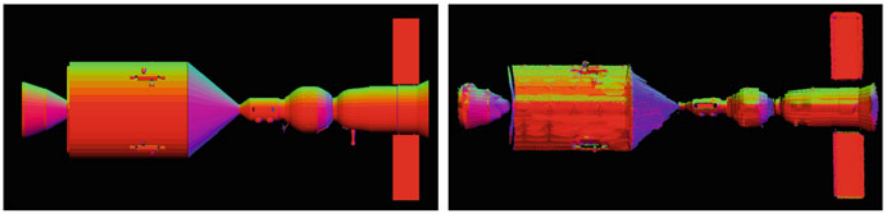

(a) True positive normal Map (b) Estimate positive normal map

Fig. 13.31 A comparison of true positive normal map and estimated positive normal map of spacecraft model rendered with specular reflection

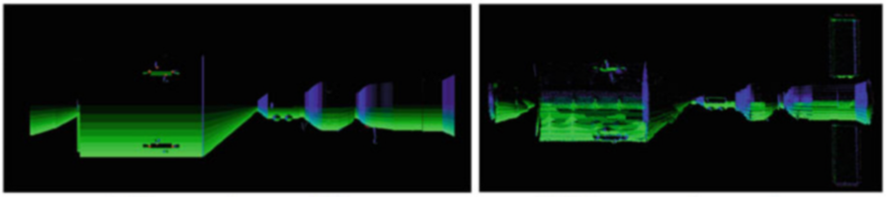

(a) True negative normal Map (b) Estimate negative normal map

Fig. 13.32 A comparison of true negative normal map and estimated negative normal map of spacecraft model rendered with specular reflection

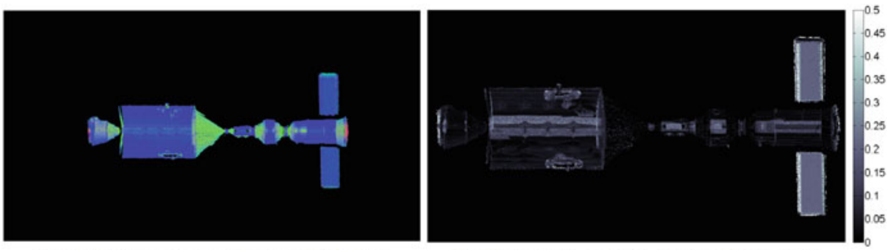

(a) Estimated normal vector uncertainty direction map (b) Estimated normal vector uncertainty magnitude map

Fig. 13.33 Standard deviation of the estimated normal vectors uncertainty (**a**) direction map (**b**) magnitude map if spacecraft model with specular reflection surface

shows that the estimation result is relatively poor in comparison to the estimates obtained from the idealized case where the reflectance is a pure Lambertian surface. This is because RANSAC cannot remove all the measurement hypotheses that have specularity. Developing a better method to remove specular reflection has been a active study in the research community. Methods such as SUV color space transform [25] and specular free image [35] are developed for this purpose. However, most of these methods require color information. Man-made spacecraft are typically textureless and theses methods are not directly applicable. Currently,

Fig. 13.34 Estimate surface depth standard deviation map of spacecraft model with specular reflection

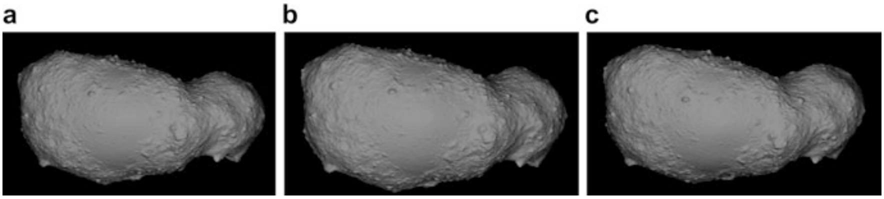

Fig. 13.35 3 out of 50 measurements of Itokawa model rendered by Oren Nayar model

removing specular with RANSAC remains the most popular method that applicable to general surface.

Natural space objects such as asteroid generally have a relatively diffuse surface, while carrying weak directional reflection properties like specular reflection. Oren-Nayar model [28] is a diffuse model that is developed to model such weak directionally diffuse reflection on a rough surface. The Lambertian approach can serve as an approximation to Oren-Nayar surface when surface roughness is removed. Therefore, we are directly supplying measurement generated from Oren-Nayar model into proposed algorithm for surface estimation.

Figure 13.35 shows a subset of input images for Itokawa model rendered from the Oren-Nayar model. Estimation result obtained by using this data set is shown in Figs. 13.36, 13.37, 13.38, 13.39, and 13.40.

Results of estimation of the surface of the Itokawa model rendered with Oren-Nayar reflectance model show that its estimation accuracy is as good as measurement rendered with Lambertian model. The fact that the model reconstruction operations using the algorithms developed here are modestly robust to reflectance model forms a basis of optimism towards the applicability of the proposed approach to reconstruct the surfaces of weekly specular object from image data. Since the true

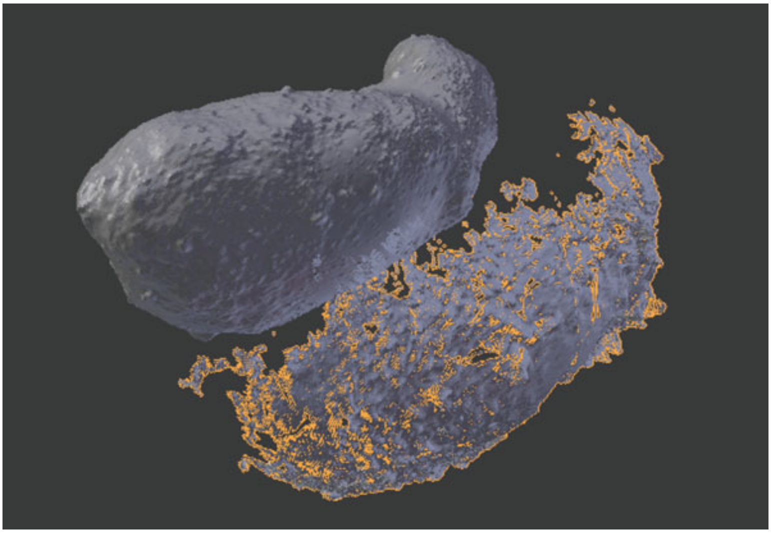

Fig. 13.36 A side to side comparison of empirically scaled Itokawa surface estimates (front) with true object surface (back) with measurement rendered with Oren-Nayar model

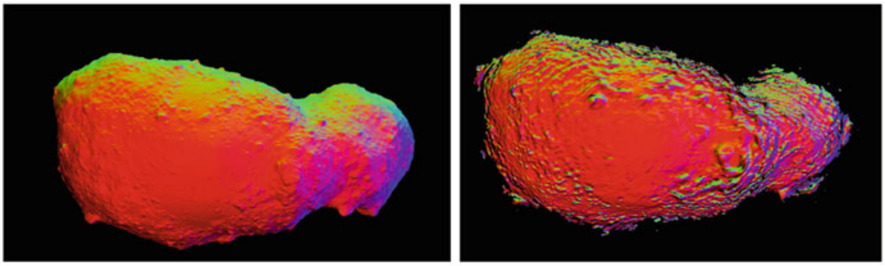

(a) True positive normal Map (b) Estimate positive normal map

Fig. 13.37 A comparison of true positive normal map and estimated negative normal map of asteroid model rendered with Oren-Nayar model

reflectance characteristics are generally unknown, the approaches discussed here-in as a part of the DDDAS for SSA applications seems promising.

13.7 Conclusion

A photometric stereopsis in motion approach for space object dense surface reconstruction based on structure from motion and photometric stereo is discussed in this Chapter. It forms an integral component of the RSO shape estimation algorithms

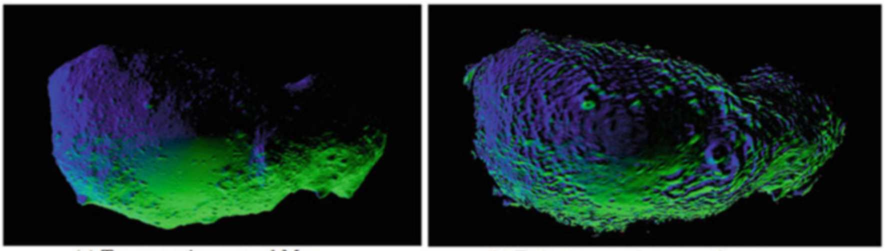

(a) True negative normal Map (b) Estimate negative normal map

Fig. 13.38 A comparison of true negative normal map and estimated negative normal map of asteroid model rendered with Oren-Nayar model

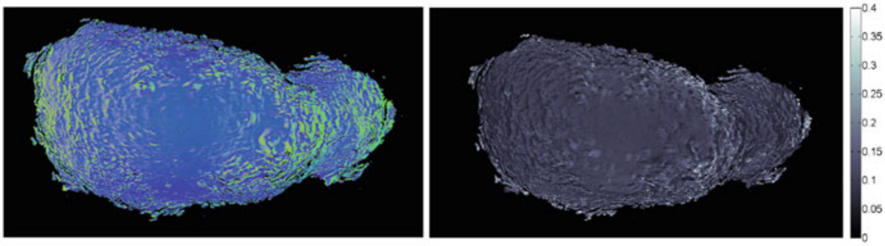

(a) Estimated normal vector uncertainty direction map (b) Estimated normal vector uncertainty magnitude map

Fig. 13.39 Estimated normal vector uncertainty standard deviation (**a**) direction map (**b**) magnitude map of asteroid model rendered with physical reflection model

Fig. 13.40 Estimate surface depth standard deviation map of asteroid model with physical reflection

in an innovative INFORM framework that is DDDAS for SSA applications. Emulation experiments utilizing two different geometry models, each representing a man-made and natural RSO are used to demonstrate the utility of photometric stereopsis algorithms under non-ideal illumination, surface reflectance and relative motion conditions. Experimental results show that the algorithms discussed are capable of providing valid surface geometry estimates even when the assumption of diffuse surface is not exactly valid. It is shown that the use of photometry for shape estimation provides an alternative to textured based stereopsis solutions that fail to produce any reconstruction in bland surfaces. Experiment results also demonstrate that the concept of using structure from motion for initialization, and then iteratively switching between surface propagation and photometric stereo is a feasible approach for dense surface reconstruction when relative motion exists between the object and the observer.

Acknowledgements This work is based upon work supported by the AFOSR grant FA9550-15-1-0313. Drs. Erik Blasch, Sai Ravella and Frederica Darema are acknowledged for the technical discussions. The authors are also grateful to the inputs of the anonymous reviewers. Their inputs enhanced the quality of the chapter extensively.

References

1. J. Ackermann, F. Langguth, S. Fuhrmann, M. Goesele, Photometric stereo for outdoor web-cams, in *IEEE Conference on Computer Vision and Pattern Recognition (CVPR), (Providence,* 2012) pp. 262–269. https://doi.org/10.1109/CVPR.2012.6247684
2. N. Alldrin, D. Kriegman, Toward reconstructing surfaces with arbitrary isotropic reflectance: A stratified photometric stereo approach, in *IEEE 11th International Conference on Computer Vision (ICCV)*, Rio de Janeiro, 2007 pp. 1–8. https://doi.org/10.1109/ICCV.2007.4408881
3. O. Barnouin, H.E. Kahn, Amica images with geometry backplanes v1.0. hay-a-amica-3-amicageom-v1.0 (2012). http://sbn.psi.edu/pds/resource/amicageom.html
4. Bouguet, J-Y., Camera calibration toolbox for matlab (2004). http://www.vision.caltech.edu/bouguetj/calib_doc/index.html.
5. M. Carbajal, Apollo Soyuz (2009). http://nasa3d.arc.nasa.gov/detail/apollo-soyuz-c
6. J.F. Cavanaugh, J.C. Smith, X. Sun, A.E. Bartels, L Ramos-Izquierdo, D.J. Krebs, J.E. McGarry, R. Trunzo, A.M. Novo-Gradac, J.L. Britt et al., The mercury laser altimeter instrument for the messenger mission, in *The Messenger Mission to Mercury* (Springer, New York, 2007), pp. 451–479
7. J.L. Crassidis, J.L. Junkins, *Optimal Estimation of Dynamic Systems* (CRC Press, Hoboken, 2011)
8. M.A. Fischler, R.C. Bolles, Random sample consensus: a paradigm for model fitting with applications to image analysis and automated cartography. Commun. ACM **24**(6), 381–395 (1981). http://doi.acm.org/10.1145/358669.358692
9. R.T. Frankot, R. Chellappa, A method for enforcing integrability in shape from shading algorithms. IEEE Trans. Pattern Anal. Mach. Intell. **10**(4), 439–451 (1988)
10. K. Gray, *Microsoft DirectX 9 Programmable Graphics Pipeline* (Microsoft Press, Redmond, 2003)
11. R. Hartley, A. Zisserman, *Multiple View Geometry in Computer Vision* (Cambridge University Press, Cambridge, 2003)

12. X.D. He, K.E. Torrance, F.X. Sillion, D.P. Greenberg, A comprehensive physical model for light reflection, in *Proceedings of the 18th Annual Conference on Computer Graphics and Interactive Techniques*, Las Vegas, 1991
13. C. Hernandez, G. Vogiatzis, R. Cipolla, Multiview potometric stereo. IEEE Trans. Pattern Anal. Mach. Intell. **30**(3), 548–554 (2008)
14. T. Higo, Y. Matsushita, N. Joshi, K. Ikeuchi, A hand-held photometric stereo camera for 3-d modeling, in *IEEE 12th International Conference on Computer Vision*, Kyoto, 2009, pp. 1234–1241. https://doi.org/10.1109/ICCV.2009.5459331
15. B. Horn, *Obtaining Shape from Shading Information* (McGraw-Hill, New York, 1975)
16. B.K. Horn, M.J.Brooks, The variational approach to shape from shading. Comput. Vis. Graph. Image Process. **33**(2), 174–208 (1986)
17. J. Immerkaer, Fast noise variance estimation. Comput. Vis. Image Underst. **64**(2), 300–302 (1996)
18. B. Jia, K.D. Pham, E. Blasch, D. Shen, Z. Wang, G. Chen, Cooperative space object tracking using space-based optical sensors via consensus-based filters. IEEE Trans. Aerosp. Electron. Syst. **52**(3), 1908–1936 (2016)
19. S.J. Julier, J.K. Uhlmann, New extension of the Kalman filter to nonlinear systems, in *AeroSense'97, International Society for Optics and Photonics*, Orlando, 1997, pp. 182–193
20. R. Klette, K. Schluens, Height data from gradient maps, in *Photonics East'96, International Society for Optics and Photonics*, 1996, pp. 204–215
21. J. Lim, J. Ho, M.H. Yang, D. Kriegman, Passive photometric stereo from motion, in *Tenth IEEE International Conference on Computer Vision, 2005. ICCV 2005*, vol. 2, Beijing, 2005, pp. 1635–1642. https://doi.org/10.1109/ICCV.2005.185
22. Z. Liu, W. Wan, M. Peng, Q. Zhao, B. Xu, B. Liu, Y. Liu, K. Di, L. Li, T. Yu, B. Wang, J. Zhou, H. Chen, Remote sensing mapping and localization techniques for teleoperation of chang'e-3 rover. J. Remote Sen. **18**(5), 971–980 (2014)
23. D. Lowe, Object recognition from local scale-invariant features, in *Proceedings of the Seventh IEEE International Conference on Computer Vision, 1999*, vol. 2, Kerkyra, 1999, pp. 1150–1157. https://doi.org/10.1109/ICCV.1999.790410
24. B.D. Lucas, T. Kanade, An iterative image registration technique with an application to stereo vision. IJCAI 81, Vancouver, Canada, (1981)
25. S.P. Mallick, T.E. Zickler, D.J. Kriegman, P.N. Belhumeur, Beyond lambert: Reconstructing specular surface using color, in *Computer Vision and Pattern Recognition, San Diego, CA* (IEEE, 2005)
26. A.S. McEwen, Photometric functions for photoclinometry and other applications. Icarus **92**(2), 298–311 (1991)
27. A. OpenGL, M. Woo, J. Neider, T. Davis, *OpenGL Programming Guide, Orlando, FL* (Addison-Wesley, Reading, 1999)
28. M. Oren, S.K. Nayar, Generalization of Lambert's reflectance model, in Proceedings of 21st Annual Conference on Computer Graphics and Interactive Technique, Orlando, (ACM, 1994)
29. M. Peng, K. Di, Z. Liu, Adaptive Markov random field model for dense matching of deep space stereo images. J. Remote Sens. **18**(1), 77–89 (2014)
30. M. Pharr, G. Humphreys, *Physically Based Rendering: From Theory to Implementation* (Morgan Kaufmann, Amsterdam, 2004)
31. R. Raskar, K.H. Tan, R. Feris, J. Yu, M. Turk, Non-photorealistic camera: depth edge detection and stylized rendering using multi-flash imaging, in *ACM Transactions on Graphics (TOG)* (ACM, New York, 2004), pp. 679–688
32. D. Scharstein, R. Szeliski, A taxonomy and evaluation of dense two-frame stereo correspondence algorithms. Int. J. Comput. Vis. **47**(1–3), 7–42 (2002)
33. H. Schaub, J.L. Junkins, *Analytical Mechanics of Space Systems* (AIAA, Reston, 2003)
34. S.M. Seitz, B. Curless, J. Diebel, D. Scharstein, R. Szeliski, A comparison and evaluation of multi-view stereo reconstruction algorithms, in *IEEE Computer Society Conference on Computer Vision and Pattern Recognition, New York City*, (IEEE, 2006)
35. R.T. Tan, K. Nishino, K. Ikeuchi, Separating reflection component based on chromaticity and noise analysis. IEEE Trans. Pattern Anal. Mach. Intell. **26**(10), 1373–1379 (2004)

36. C. Tomasi, T. Kanade, Shape and motion from image streams under orthography: a factorization method. Int. J. Comput. Vis. **9**(2), 137–154 (1992)
37. K.E. Torrance, E.M. Sparrow, Theory for off-specular reflection from roughened surface. J. Opt. Soc. Am. **57**(9), 1105–1114 (1967)
38. Y. Wang, J. Bu, N. Li, M. Song, P. Tan, Detecting discontinuities for surface reconstruction, in *21st International Conference on Pattern Recognition (ICPR), Tsukuba Science City*, (IEEE, 2012), pp. 2108–2111
39. X.I. Wong, M. Majji. Uncertainty Quantification of Lucas Kanade Feature Track and Application to Visual Odometry. Computer Vision and Pattern Recognition Workshops (CVPRW), Honolulu, HI, 2017 IEEE Conference on. IEEE, 2017.
40. L.F. Yu, S.K. Yeung, Y.W. Tai, D. Terzopoulos, T. Chan, Outdoor photometric stereo, in *IEEE International Conference on Computational Photography (ICCP)*, Jiuzhai, 2013, pp. 1–8. https://doi.org/10.1109/ICCPhot.2013.6528306
41. Z. Zhou, Z. Wu, P. Tan, Multi-view photometric stereo with spatially varying isotropic materials, in *IEEE Conference on Computer Vision and Pattern Recognition (CVPR), Portland*, (IEEE, 2013), pp. 1482–1489